PHYSICAL REVIEW D VOLUME 6, NUMBER 1 1 JULY 1972

Study of $|T_z|=3/2$ $\Delta(1238)$ Production in pp Interactions at 6.6 GeV/c*

Eugene Colton and Alan R. Kirschbaum
Lawrence Berkeley Laboratory, University of California, Berkeley, California 94720

(Received 6 March 1972)

$|T_z|=\frac{3}{2}$ $\Delta(1238)$ systems are studied from the standpoint of direct production utilizing experimental data on the reactions $pp\rightarrow p\pi^+n$, $pp\rightarrow p\pi^+\pi^-p$, $pp\rightarrow p\pi^+\pi^-\pi^0p$, and $pp\rightarrow p\pi^+\pi^-\pi^+n$. Resonance-production total and differential cross sections are presented, in addition to the decay density-matrix elements. It is demonstrated that the experimentally defined $\Delta(1238)$ systems are not characterized solely by spin-parity $\frac{3}{2}^+$, and that corresponding elements of the density matrices of both $p\pi^+$ and π^-n cases generally behave in a similar manner with increasing c.m. angle. Additional detailed studies of the t-channel moments are presented for peripherally produced πN systems as a function of both c.m. angle and πN invariant mass. Dynamical differences are observed between the $p\pi^+$ and $n\pi^-$ moments for the very peripheral data. One-pion-exchange-model predictions are compared with the peripheral $p\pi^+$ moments and with several invariant-mass distributions from the $pp\rightarrow p\pi^+\pi^-p$ data. Complications arising from the presence of two $p\pi^+$ combinations in the four- and five-body final-state data are discussed.

I. INTRODUCTION

Although $\Delta(1238)$ resonance production has been investigated for more than 10 years in nucleon-nucleon collisions, there have been few attempts to understand it collectively in different final states. Several recent studies[1-3] of the systems recoiling from a $\Delta^{++}(1238)$ in four- and five-body final states have suggested a common single-pion-exchange production mechanism for small values of the momentum transfer to the $\Delta^{++}(1238)$. However, a detailed analysis of production and decay systematics of $\Delta(1238)$ production (by itself) in proton-proton collisions is currently lacking.

In this work we explore the characteristics of the more background-free $|T_z|=\frac{3}{2}$ πN systems[4] as observed in the reactions

$$pp\rightarrow p\pi^+n\,, \tag{1.1}$$

$$pp\rightarrow p\pi^+\pi^-p\,, \tag{1.2}$$

$$pp\rightarrow p\pi^+\pi^-\pi^0p\,, \tag{1.3}$$

$$pp\rightarrow p\pi^+\pi^-\pi^+n \tag{1.4}$$

at 6.6-GeV/c incident laboratory beam momentum. We restrict the study to low-invariant-mass πN systems, and consider these data as a function of center-of-mass (c.m.) angle rather than as a function of the squared four-momentum transfer t. The detailed behavior of the recoiling systems in reactions (1.2)–(1.4) is not considered here, for the sake of brevity. However, a casual look is given to the π^-p and $\pi^-\pi^+p$ invariant-mass spectra of reaction (1.2) in the closing paragraphs.

In Sec. II we first describe the data used in this analysis; then we determine the partial cross sections for $|T_z|=\frac{3}{2}$ $\Delta(1238)$ production in reactions (1.1)–(1.4). The distributions of c.m. angle and recoiling-mass spectra [in reactions (1.2)–(1.4)] are presented for the $\Delta(1238)$ events in Sec. III. The $\Delta(1238)$ decays are studied in terms of the s- and t-channel decay density-matrix elements in Sec. IV for all c.m. angles. Peripheral πN t-channel moments are presented as a function of πN mass in Sec. V; possible theoretical interpretations are discussed. In Sec. VI we study the effects of having two $p\pi^+$ combinations in a reaction by utilizing one-pion-exchange- (OPE-) model calculations. Then as a follow-up to our previous work[2] on reaction (1.2) we compare in Sec. VII the OPE-model predictions to both π^-p and $\pi^-\pi^+p$ invariant-mass spectra. Our conclusions are stated in Sec. VIII.

II. EXPERIMENTAL DATA

The numbers of events representing reactions (1.1)–(1.4), inclusive, are listed together with the respective cross sections in Table I. These events were photographed in the fall of 1965 in the Lawrence Radiation Laboratory 72-in. liquid-hydrogen bubble chamber which was exposed to a 6.6-GeV/c proton beam.[5] Information relating to scanning, measuring, and hypothesis separation has been presented in several earlier works.[2,6]

At this point we adopt a shorter notation for reaction identification which endures for the duration of this work. Henceforth, we refer to reaction (1.i) as Ri, e.g., reaction (1.1) is identified as R1.

The $|T_z|=\frac{3}{2}$ πN invariant-mass spectra for R1–R4 are presented in Figs. 1(a)–1(e). The data in Figs. 1(a)–1(d) are $M(\pi^+p)$ spectra from R1–R4, respectively; Fig. 1(e) displays the $M(\pi^-n)$ spectrum of R4. Each of the distributions in Fig. 1 is dominated by a peak at the $\Delta(1238)$ resonance position. The R1–R3 data have each been fitted to incoherent superpositions of phase space and Breit-Wigner functions of the form[7]

$$f_{\mathrm{BW}}(M)=\frac{M\Gamma(M)}{q}\,\frac{q_0\Gamma_0M_0}{(M_0{}^2-M^2)^2+M_0{}^2\Gamma^2(M)}\,, \tag{2.1}$$

where Γ represents the width at a mass M (of a $|T_z|=\frac{3}{2}$ πN system); M_0 is the resonance central position and q is the decay momentum in the resonance rest system. For an s-wave resonance Γ was assumed to be energy-independent ($=\Gamma_0$), and for a resonance of angular momentum l we take[7]

$$\Gamma(M)=\Gamma_0\left(\frac{q}{q_0}\right)^{2l+1}\frac{\rho(M)}{\rho(M_0)}\,, \tag{2.2}$$

where $\rho(M)=(\mu^2+q^2)^{-1}$ and μ is the pion rest mass. The fit to the R4 data is similar to those for R1–R3 but involves an additional product of Breit-Wigner functions for simultaneous $\Delta^{++}(1238)$, $\Delta^{-}(1238)$ production.

The actual fits utilized the maximum-likelihood method[8] together with the program OPTIME.[9] Each of R1–R4 required a p-wave Breit-Wigner function corresponding to the $\Delta(1238)$; R1 required an additional $\Delta(\sim1900)$ contribution (assumed s wave in fit). No considerations were given to possible cascade decays, resonances in nonpure πN isospin systems, resonances in the recoiling systems in R2 and R3, t-dependent effects, or interferences, even though they are clearly necessary.[10] In Fig. 2(a) we display the experimental $M(p_1\pi^+)$ vs $M(p_2\pi^+)$ plot for R2 (i.e., $pp\rightarrow p_1\pi^+\pi^-p_2$); the overlapping $\Delta^{++}(1238)$ bands can be treated correctly (at least at 6.6 GeV/c) only by a model which considers interfering $\Delta^{++}(1238)$ resonances. Similar statements apply to R3 and R4, of course. In the fits to the R2–R4 data we treat the two $p\pi^+$ combinations as equal events. Figure 2(b) displays the $M(p\pi^+)$ vs $M(\pi^-n)$ plot for R4; the overlapping bands indicate a substantial fraction of $\Delta^{++}(1238)$, $\Delta^{-}(1238)$ production. Thus, in the case of R4, the fitting function was a sum of four incoherent parts: phase space, $\Delta^{++}(1238)$ production, $\Delta^{-}(1238)$ production, and simultaneous $\Delta^{++}(1238)$, $\Delta^{-}(1238)$ production.

TABLE I. Data used in the analysis of proton-proton interactions at 6.6 GeV/c.

Reaction	Number of events	Cross section (mb)
$pp\rightarrow p\pi^+n$	6423	5.73 ± 0.35
$pp\rightarrow p\pi^+\pi^-p$	7504	2.70 ± 0.16
$pp\rightarrow p\pi^+\pi^-\pi^0p$	6098	2.15 ± 0.13
$pp\rightarrow p\pi^+\pi^-\pi^+n$	7302	2.47 ± 0.15

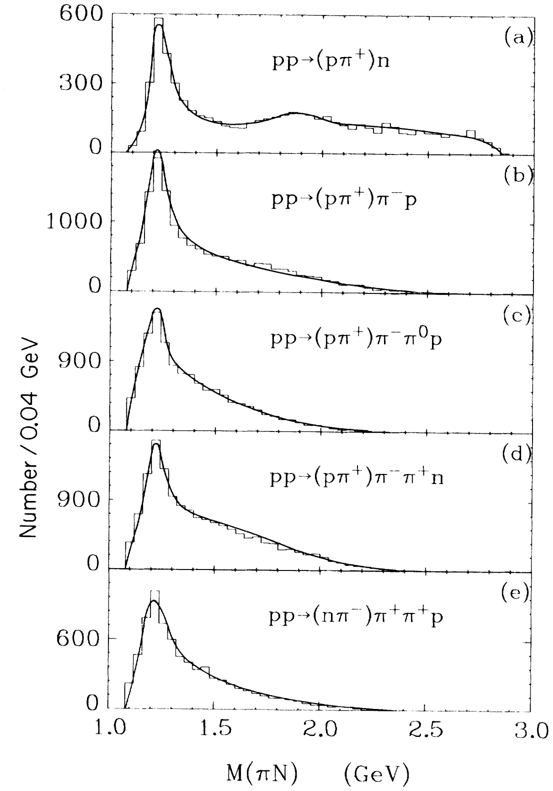

FIG. 1. (a)–(e) The five possible invariant-mass spectra for πN systems (bracketed) with z component of isotopic spin (T_z) equal to $\pm\frac{3}{2}$, in reactions (1.1)–(1.4) (R1–R4). Two combinations are plotted for each event in (b), (c), and (d). The smooth curves superimposed upon the data represent the results of maximum-likelihood fits which are described in Sec. II.

The fit results, which include best fit masses and widths as well as partial fractions[11] and cross sections for the Δ production processes, are listed in Table II. The best fit $\Delta(1238)$ masses and widths are consistent with the accepted values[12] except

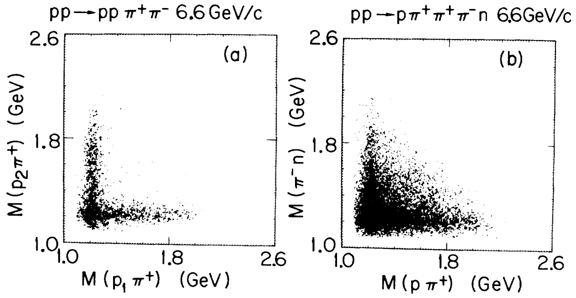

FIG. 2. (a) Experimental distribution of $M(p_1\pi^+)$ vs $M(p_2\pi^+)$ for the 7504 examples of $pp\rightarrow p_1\pi^+\pi^-p_2$. (b) Experimental distribution of $M(p\pi^+)$ vs $M(\pi^-n)$ for the 7302 examples of $pp\rightarrow p\pi^+\pi^-\pi^+n$. Both $p\pi^+$ combinations are plotted for each event.

TABLE II. Results of maximum-likelihood fits to R1–R4 data as described in Sec. II.

Best-fit quantity	Reaction R1	R2	R3	R4
$M(\Delta^{++}(1238))$ (GeV)	1.236±0.002	1.226± 0.002	1.222± 0.003	1.226± 0.002
$M(\Delta^{++}(1900))$ (GeV)	1.86	···	···	···
$M(\Delta^{-}(1238))$ (GeV)	···	···	···	1.239± 0.005
$\Gamma_0(\Delta^{++}(1238))$ (GeV)	0.115± 0.006	0.127± 0.005	0.122± 0.009	0.106± 0.007
$\Gamma_0(\Delta^{++}(1900))$ (GeV)	0.18	···	···	···
$\Gamma_0(\Delta^{-}(1238))$ (GeV)	···	···	···	0.237± 0.022
fraction of $\Delta^{++}(1238)$ (%)	35.1 ± 0.8	82.6 ± 0.8	55.9 ± 1.2	21.1 ± 1.6[a]
fraction of $\Delta^{++}(1900)$ (%)	7.2 ± 0.8	···	···	···
fraction of $\Delta^{-}(1238)$ (%)	···	···	···	22.9 ± 1.6[b]
fraction of simultaneous $\Delta^{++}(1238)\Delta^{-}(1238)$ (%)	···	···	···	28.5 ± 1.5
$\sigma(\Delta^{++}(1238))$ (mb)	2.01 ± 0.13	2.23 ± 0.13	1.19 ± 0.08	0.52 ± 0.05[a]
$\sigma(\Delta^{++}(1900))$ (mb)	0.41 ± 0.05	···	···	···
$\sigma(\Delta^{-}(1238))$ (mb)	···	···	···	0.56 ± 0.05[b]
$\sigma(\Delta^{++}(1238)\Delta^{-}(1238))$ (mb)	···	···	···	0.70 ± 0.06

[a] Includes no $\Delta^{-}(1238)$ production.
[b] Includes no $\Delta^{++}(1238)$ production.

for the $\Delta^{-}(1238)$ width (Γ_0) of ~240 MeV; this appears to be due to the insensitivity of the observed width [not $\Gamma(M)$] of the Breit-Wigner function [Eq. (2.1)] to Γ_0 as Γ_0 increases to above 100 MeV. Apparently some complex reflection(s) slightly steepens the leading edge and/or skews the shape of the $M(n\pi^-)$ distribution, thereby resulting in a large fitted value for Γ_0. Unfortunately this effect precludes a dependable measurement of the Δ^{++}-Δ^{-} mass difference using the data of R4. Table II also indicates that $\Delta^{++}(1238)$ production dominates R2 (~80%) and decreases to ~55% and ~50% for R3 and R4, respectively. In addition, an approximately equal portion of $\Delta^{-}(1238)$ production (~50%) is obtained for R4. Finally, curves representing the normalized predictions of the fits are superimposed upon the data in Figs. 1(a)–1(e). These curves describe the histograms well, as expected.

III. Δ(1238) RESONANCE PRODUCTION

In order to assure an enriched sample of $\Delta(1238)$ events for further analysis we select resonant events by an invariant-mass slice in the $|T_z|=\frac{3}{2}$ πN system:

$$1.16 < M(\pi N) < 1.30 \text{ GeV}. \qquad (3.1)$$

The numbers of R1–R4 events surviving this cut are listed in Table III along with the nonresonant background percentages expected in the same slice (from the fits described in Sec. II). The background percentages vary strongly with production angle and are least for small angles. Since this analysis deals most with small-angle events, no background corrections are performed. Table III also lists for R2–R4 the number of events with both $M(p\pi^+)$ combinations occurring inside the cut (3.1). In nearly all subsequent distributions we

TABLE III. Events with $|T_z|=\frac{3}{2}$ πN masses occurring within the range $1.16 < M(\pi N) < 1.30$ GeV.

Reaction–(system)	Events within range	Events with both combinations in range	Nonresonant background in range (%)
R1–($p\pi^+$)	1477	···	12
R2–($p\pi^+$)	4604	691	31
R3–($p\pi^+$)	3683	697	35
R4–($p\pi^+$)	4120	590	30
R4–($n\pi^-$)	2844	···	27

treat all $M(p\pi^+)$ combinations as events with equal weight; thus events will sometimes appear twice.

In Figs. 3(a)–3(e) we present the center-of-mass (c.m.) angular distributions for the five $|T_z|=\frac{3}{2}$ $\Delta(1238)$ cases. As mentioned above, if both $M(p\pi^+)$ combinations for an event occur within the cut (3.1), then the c.m. angles of both combinations are used with equal weight (one). All of the distributions display a sharp forward peaking, which indicates a dominant peripheral production of $\Delta(1238)$ resonances. Figure 3 also illustrates that the degree of peripherality depends most strongly upon the number of final-state particles: The steepest distribution occurs for the three-body final state (R1).

The term, peripheral, is synonymous with small values of t, the four-momentum-transfer squared from an initial-state proton to the outgoing πN system. In Fig. 4 we show the kinematic correspondence between the c.m. angle (θ), t, and $M(p\pi^+)$ for R1. For $M^2(p\pi^+) < 5$ GeV^2, small-angle cuts are equivalent to small t cuts. In the case of R2–R4 a dependence upon the recoiling masses [e.g., $M(p\pi^-)$ for R2] additionally enters into the relationship between θ and t.

The invariant-mass spectra of the systems recoiling against the $|T_z|=\frac{3}{2}$ $\Delta(1238)$ resonances in R2–R4 are presented in Figs. 5(a)–5(d), inclusive. Clear resonance production is apparent in Fig. 5(a) at the positions of the well-known $\Delta^0(1238)$, $N^{*0}(1512)$, and $N^{*0}(1688)$ positions, and in Fig. 5(c) near 1700 MeV. No statistically significant enhancements are apparent in the $T_z=\frac{5}{2}$ $M(p\pi^+\pi^+)$ spectrum in Fig. 5(d). The crosshatched histograms in Fig. 5 represent the peripheral component with $\theta < 20°$ [θ is the c.m. angle of the $\Delta(1238)$]. The signal to background ratios of the enhancements in Figs. 5(a) and 5(c) are increased for the peripheral events. In fact, the nonperipheral component with $\theta \geq 20°$ displays little resonance structure. Thus, Fig. 5 suggests that (for R2–R4) the peripherally produced $T_z=\frac{3}{2}$ $\Delta(1238)$ resonances may be produced directly with other (sometimes resonant) systems.

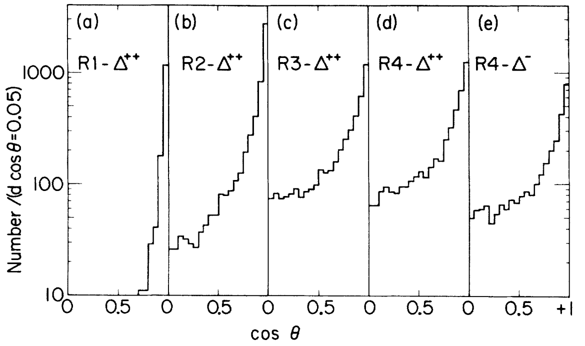

FIG. 3. Experimental c.m. angular distributions of the five indicated $|T_z|=\frac{3}{2}$ $\Delta(1238)$ systems, where the $\Delta(1238)$ events are defined by the invariant-mass slice of Eq. (3.1). θ is the angle between the outgoing πN system and that initial-state proton which propagates in the same hemisphere in the c.m. system.

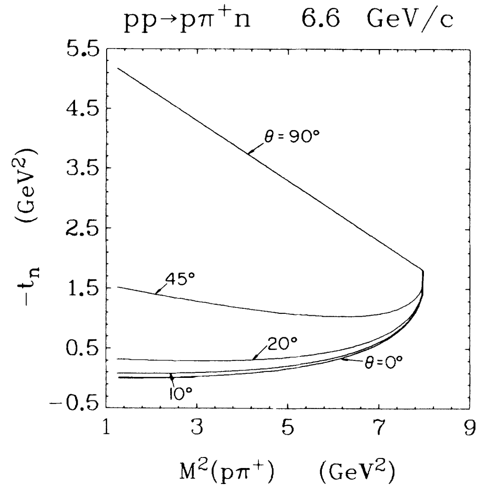

FIG. 4. Kinematic correspondences of $M^2(p\pi^+)$ vs invariant four-momentum transfer squared to the neutron (t_n) for R1 at 6.6 GeV/c. The denoted curves represent lines of constant c.m. angle θ.

IV. Δ(1238) DECAY

Further information can be obtained about the $\Delta(1238)$ resonance production by studying the decay

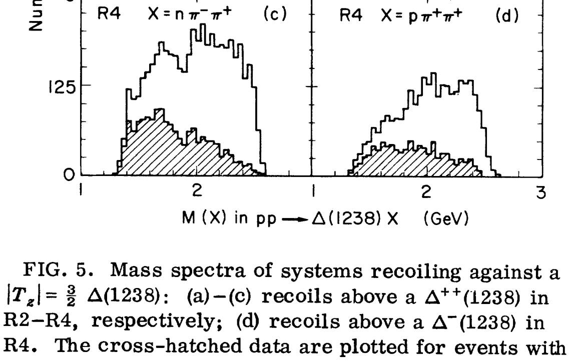

FIG. 5. Mass spectra of systems recoiling against a $|T_z|=\frac{3}{2}$ $\Delta(1238)$: (a)–(c) recoils above a $\Delta^{++}(1238)$ in R2–R4, respectively; (d) recoils above a $\Delta^-(1238)$ in R4. The cross-hatched data are plotted for events with c.m. angle $\theta < 20°$.

of the isobar into $N\pi$. The decay of a spin-$\frac{3}{2}$ isobar into a spin-$\frac{1}{2}$ nucleon and a spin-0 pion is given by the normalized distribution[13]

$$W(\alpha,\beta) = \frac{1}{4\pi}[1 + (\tfrac{4}{5}\pi)^{1/2}(1-4\rho_{33})Y_2^0 - 8(\tfrac{2}{5}\pi)^{1/2}(\mathrm{Re}\rho_{3,-1}\,\mathrm{Re}Y_2^2 - \mathrm{Re}\rho_{3,1}\,\mathrm{Re}Y_2^1)], \tag{4.1}$$

where the Y_L^M are spherical harmonic functions with arguments α and β. α and β represent the polar and azimuthal angles, respectively, of the decay nucleon expressed in the standard[14] s- or t-channel coordinate system. The ρ_{ij} are the decay density-matrix elements. Orthonormality of the Y_L^M functions leads to the determination of the density-matrix elements:

$$\rho_{33} = \tfrac{1}{4}(1 - \sqrt{20\pi}\,\langle Y_2^0\rangle),$$

$$\mathrm{Re}\rho_{3,-1} = -(\tfrac{5}{2}\pi)^{1/2}\langle \mathrm{Re}Y_2^1\rangle,$$

and (4.2)

$$\mathrm{Re}\rho_{3,1} = (\tfrac{5}{2}\pi)^{1/2}\langle \mathrm{Re}Y_2^2\rangle,$$

where

$$\rho_{33} + \rho_{11} = \tfrac{1}{2}.$$

In Fig. 6 we display the t-channel decay density-matrix elements for each of the five $|T_z| = \frac{3}{2}$ Δ(1238) resonances, plotted as a function of the c.m. angle θ.[15] Those events of R2–R4 where both $M(p\pi^+)$ combinations satisfied the cut (3.1) were used with weight $\cos\theta_i/(\cos\theta_1 + \cos\theta_2)$ where i represents the ith $p\pi^+$ combination.[16] Corresponding elements for the five different Δ(1238) samples are strikingly similar: The ρ_{33} are all positive and increase from a small value at $\theta = 0$ to approximately 0.25 at $\theta = 90°$; with the exception of the R1 data the $\mathrm{Re}\rho_{3,1}$ are generally small and negative, and the $\mathrm{Re}\rho_{3,-1}$ are consistent with zero. Similar behavior is also observed in the case of the s-channel decay density-matrix elements (not shown here), but the $\mathrm{Re}\rho_{3,1}$ elements all appear to be positive.

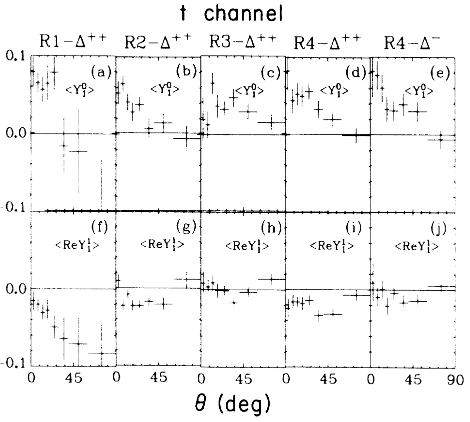

FIG. 7. θ dependence of the t-channel moments of the decay nucleon angular distribution, evaluated in the Δ(1238) rest system: (a)–(e) $\langle Y_1^0\rangle$; (f)–(j) $\langle \mathrm{Re}Y_1^1\rangle$.

If the Δ^{++}(1238) resonances in R1–R4 were to be produced directly via a spin-0 exchange process then all of the Δ^{++}(1238) density-matrix elements plotted in Fig. 6 would be identically zero[17] (if we ignore the effects of two $p\pi^+$ combinations in R2–R4). Excepting R1, the Δ^{++}(1238) ρ_{ij} show qualitatively this trend at small angles. Similar results for the Δ^-(1238) resonance (in R4) are ambiguous in that exchange of a charged −2 system is neces-

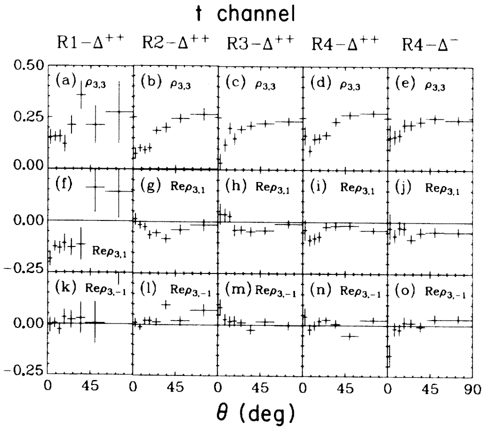

FIG. 6. Δ(1238) resonance decay density-matrix elements plotted vs c.m. angle θ. The experimental points are calculated utilizing Eqs. (4.2) in the t-channel coordinate system: (a)–(e) ρ_{33}; (f)–(j) $\mathrm{Re}\rho_{3,1}$; (k)–(o) $\mathrm{Re}\rho_{3,-1}$.

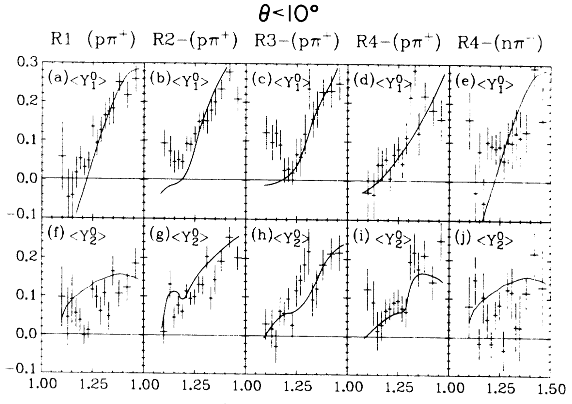

FIG. 8. t-channel moments of the angular distribution of the outgoing nucleon (N) evaluated in the rest frame of the denoted $N\pi$ system. The data are plotted as a function of $M(N\pi)$ for $N\pi$ combinations with $\theta < 10°$. (a)–(e) $\langle Y_1^0\rangle$; (f)–(j) $\langle Y_2^0\rangle$. The smooth curves are described in Sec. V B.

sary for direct production.

We must point out that a serious interpretation of all the data in Fig. 6 is impossible at this time without consideration of absorption effects,[18] wrong $p\pi^+$ combinations, Reggeization, off-mass-shell effects, interferences, etc. In fact, another complication is due to the presence in our $\Delta(1238)$ data of spin parities other than $\frac{3}{2}^+$. In Fig. 7 we display the t-channel moments of $\langle Y_1^0\rangle$ and $\langle \mathrm{Re}Y_1^1\rangle$, plotted again as a function of c.m. angle θ, for the five $|T_z| = \frac{3}{2}$ $\Delta(1238)$ systems. These moments are expected[17] to be zero for a pure spin-$\frac{3}{2}$ $\Delta(1238)$ decay. Nonzero $\langle Y_1^0\rangle$ terms imply an s-p wave interference, thus the presence of s waves in our "$\Delta(1238)$ data." The corresponding s-channel moments (not shown here) display a similar behavior.

V. PERIPHERAL t-CHANNEL MOMENTS

In this section we study further the $|T_z| = \frac{3}{2}$ "$\Delta(1238)$" t-channel moments as a function of $M(\pi N)$ for the peripheral data with $\theta < 20°$. This procedure adds more illumination to the s-p interference and to the apparently similar character of the $\Delta^{++}(1238)$ and $\Delta^-(1238)$ decay density-matrix elements. The data are first presented in the mass range 1.08–1.48 GeV in two 10° bins in θ; in the case of R2–R4 both $p\pi^+$ combinations are considered equally in the calculation of the moments. Then the π^+p moments are compared with the predictions of a one-pion-exchange (OPE) model calculation.

A. Experimental Moments

In Fig. 8 we display $\langle Y_1^0\rangle$ and $\langle Y_2^0\rangle$ moments for the five indicated $|T_z| = \frac{3}{2}$ πN systems as a function of $M(\pi N)$ for $\theta < 10°$. Of particular interest are the positive $\langle Y_1^0\rangle$ of R2 and R3 below 1.15 GeV, and the now significant difference between the $T_z = +\frac{3}{2}$ and $T_z = -\frac{3}{2}$ $\langle Y_1^0\rangle$ data: Each of the four $p\pi^+$ moments increases with mass above 1.15 GeV; the $n\pi^-$ data are roughly constant over the $\Delta^-(1238)$ mass region. The $\langle Y_2^0\rangle$ moments in Figs. 8(f)–8(j) also display an increasing trend with apparent discontinuities near 1.24 GeV in Fig. 8(f) and 1.30 GeV in Fig. 8(i). Figure 9 displays the distributions corresponding to those of Fig. 8 for 10°

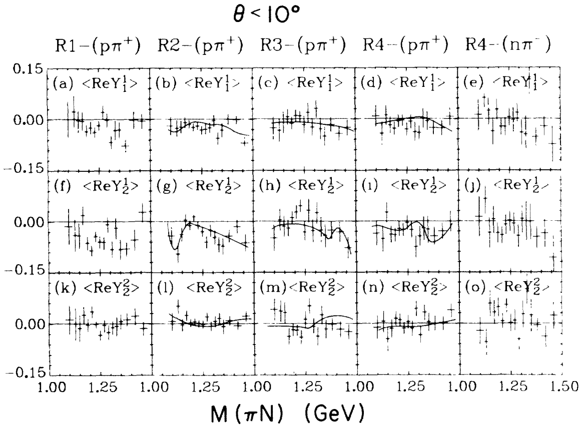

FIG. 10. t-channel moments of the angular distribution of the outgoing nucleon (N) evaluated in the rest frame of the denoted $N\pi$ system. The data are plotted as a function of $M(N\pi)$ for $N\pi$ combinations with $\theta < 10°$. (a)–(e) $\langle \mathrm{Re}Y_1^1\rangle$; (f)–(j) $\langle \mathrm{Re}Y_2^1\rangle$; (k)–(o) $\langle \mathrm{Re}Y_2^2\rangle$. The smooth curves represent corresponding predictions of OPE-model calculations described in Sec. V B.

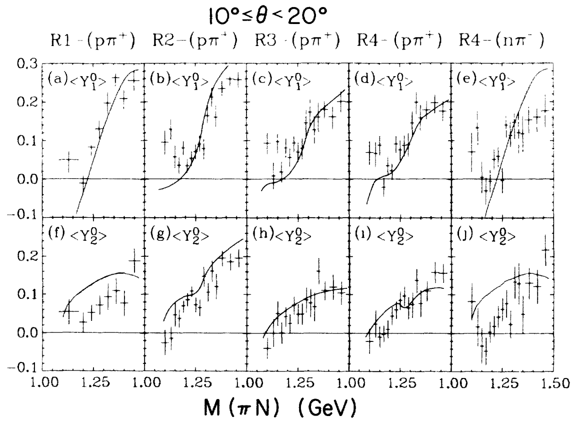

FIG. 9. t-channel moments of the angular distribution of the outgoing nucleon (N) evaluated in the rest frame of the denoted $N\pi$ system. The data are plotted as a function of $M(N\pi)$ for $N\pi$ combinations with $10° \leq \theta < 20°$. (a)–(e) $\langle Y_1^0\rangle$; (f)–(j) $\langle Y_2^0\rangle$. The smooth curves are described in Sec. V B.

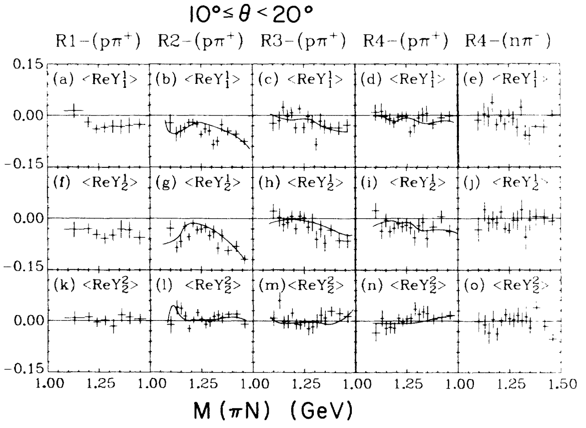

FIG. 11. t-channel moments of the angular distribution of the outgoing nucleon (N) evaluated in the rest frame of the denoted $N\pi$ system. The data are plotted as a function of $M(N\pi)$ for $N\pi$ combinations with $10° \leq \theta < 20°$. (a)–(e) $\langle \mathrm{Re}Y_1^1\rangle$; (f)–(j) $\langle \mathrm{Re}Y_2^1\rangle$; (k)–(o) $\langle \mathrm{Re}Y_2^2\rangle$. The smooth curves represent corresponding predictions of the OPE-model calculations described in Sec. V B.

$\leq\theta<20°$. The $n\pi^-$ $\langle Y_1^0\rangle$ in Fig. 9(e) now increase over the $\Delta^-(1238)$ mass region and are not qualitatively different from the corresponding data above 1.15 GeV in Figs. 9(a)–9(d).

The nonzero M moments $\langle \mathrm{Re}Y_1^1\rangle$, $\langle \mathrm{Re}Y_2^1\rangle$, and $\langle \mathrm{Re}Y_2^2\rangle$ are presented in Figs. 10 and 11 for $\theta<10°$, and $10°\leq\theta<20°$, respectively. The $\langle \mathrm{Re}Y_L^1\rangle$ are generally negative and the $\langle \mathrm{Re}Y_2^2\rangle$ are consistent with zero. Noteworthy are the apparent maxima in $\langle \mathrm{Re}Y_L^1\rangle$ near 1.23 GeV for R2. The $\langle \mathrm{Im}Y_L^M\rangle$ (not shown here) are all consistent with zero, as required by parity conservation.[19]

B. Theoretical Interpretation

Of course a serious analysis of even the peripheral moments depicted in Figs. 8–11 is impossible at this time due to the reasons given in the last paragraph of Sec. IV. However, certain trends in the data (described above in Sec. V A) lend themselves to simple interpretation. For example, the nonzero structured $\langle Y_1^0\rangle$ suggest the presence of partial waves with J^P other than $\frac{3}{2}^+$ for $|T_z|=\frac{3}{2}$ πN systems; similar behavior has been observed in π^+p (or π^-n) elastic scattering experiments. Thus, the simplest interpretation for these peripheral data is in terms of the one-pion-exchange process[20] depicted in Fig. 12. An off-mass-shell pion exchanged between the incoming protons scatters elastically at the upper vertex; X represents the recoiling systems observed in R1–R4.

The simplest OPE predictions for R1 are shown as the smooth curves in parts (a) and (f) of both Figs. 8 and 9. These curves just represent known π^+p elastic scattering data; the curves were drawn through points calculated from the CERN phase shifts.[21] The $\langle Y_1^0\rangle$ data are remarkably well reproduced by the curves, except at low $M(p\pi^+)$ (Ref. 22); the $\langle Y_2^0\rangle$ data occur below the curves, however.[23] In addition, the $\langle \mathrm{Re}Y_L^1\rangle$ data for R1, which are plotted in Figs. 10 and 11, are not accommodated by simple OPE predictions (zero). We point out that a previous pole-extrapolation analysis[24] demonstrated that the peripheral R1 data were well accounted for by the OPE process depicted in Fig. 12, possibly modified by absorption effects.

An interesting comparison can be made using the $n\pi^-$ moments of R4 in Figs. 8 and 9: The smooth curves drawn are identical to those presented for R1 and represent π^-n elastic scattering. However, the $n\pi^-$ system cannot be produced directly via OPE (as in Fig. 12) because two units of charge are required for the exchanged particle(s). The data in Fig. 8(e) are clearly inconsistent with the curve (as expected), indicating that the apparently successful fit of the curves to the R1 data in Figs. 8(a) and 9(a) is not simply due to some "universal" $\langle Y_1^0\rangle$ mass dependence for very peripheral $N\pi$ systems. The situation in Fig. 9(e) does suggest some common behavior for less peripheral data, however.

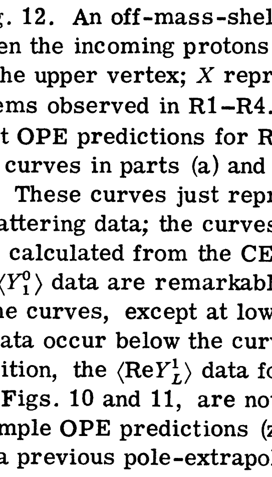

FIG. 12. One-pion-exchange process for $pp\rightarrow(p\pi^+)+X$.

We turn now to the $p\pi^+$ moments for R2–R4, inclusive. These reactions have two $p\pi^+$ combinations. When utilizing a particular $p\pi^+$ combination in the determination of an experimental $\langle Y_L^M\rangle$ point, we have no knowledge, *a priori*, to ascertain if that combination is the correct one.[25] Therefore, a thorough theoretical comparison requires consideration of the process indicated in Fig. 12 and its partner where outgoing π mesons are interchanged between vertices, as well as their mutual interference term. In the following analysis we ignore the interference term contributions in order to preserve a simplistic approach.[26] In order to calculate the theoretical OPE predictions to the $\langle Y_L^M\rangle$ moments depicted in Figs. 8–11, events were generated by a Monte Carlo technique[27] utilizing preferred phase-space generation; these events were weighted according to the amplitude for the process depicted in Fig. 12. Then each $p\pi^+$ combination was tested separately, just as in the real data; this total procedure is equivalent to considering the sum of both diagrams (mentioned above) incoherently. The OPE-model calculations are described in the Appendix.

The OPE-model predictions for the $p\pi^+$ $\langle Y_1^0\rangle$ and $\langle Y_2^0\rangle$ moments are represented by the smooth curves in parts (b)–(d) and (g)–(i) of Figs. 8 and 9. The $\langle Y_1^0\rangle$ data in Figs. 8(b) and 8(c) are well described above 1.15 GeV by the curves, as are the $\langle Y_1^0\rangle$ of R4 over the entire $M(p\pi^+)$ region. The $\langle Y_2^0\rangle$ data in Figs. 8(g)–8(i) are also described fairly well, even at the discontinuity near 1.3 GeV in Fig. 8(i). In addition, the curves in Figs. 9(b)–9(d) also adequately represent the $\langle Y_1^0\rangle$ data above 1.15 GeV, as well as reproducing the general trend of the $\langle Y_2^0\rangle$ data in Figs. 9(g)–9(i).

Even more impressive are the curves drawn in Figs. 10 and 11 describing the $\langle \mathrm{Re}Y_L^M\rangle$ moments for the $p\pi^+$ data of R2–R4: The maxima at ~1.23 GeV for the R2 $\langle \mathrm{Re}Y_L^1\rangle$ moments are fit well by the OPE-model predictions. Moreover, the R3 and R4 $\langle \mathrm{Re}Y_L^M\rangle$ data are also well described by the OPE predictions. We point out that an OPE model not incorporating two-combination considerations will predict zero for the $\langle \mathrm{Re}Y_L^M \rangle$ moments. In addition, an absorption modified OPE model considering only one combination would not be expected to yield the detailed $M(p\pi^+)$ dependences, as observed in Fig. 10(g).

VI. WRONG-COMBINATION EFFECTS

Continuing the OPE analysis explained above and in the Appendix, we show in Fig. 13 the predicted fraction of wrong $p\pi^+$ combinations[25] as a function of $M(p\pi^+)$ and θ for R2. Both $p\pi^+$ combinations for each Monte Carlo event were tested against the c.m. angle (θ) cuts indicated, and the ratios of wrong combinations to total combinations occurring within the selected θ range were plotted as a function of $M(p\pi^+)$. Figure 13 indicates that the fraction of wrong combinations is smallest for very peripheral $p\pi^+$ systems near 1.23 GeV. Alternately "contamination" from wrong combinations is expected to become substantial as one moves away from the central position of the $\Delta^{++}(1238)$ peak. We predict similar behavior in the cases of R3 and R4.

The particular $M(p\pi^+)$ structure in the $\langle \mathrm{Re}Y_L^1 \rangle$ data in parts (b) and (h) of Figs. 10 and 11 is well described by the above simple interpretation: The apparent maximum (~zero) occurs where wrong combination effects are minimal [near $M(p\pi^+) = 1.23$ GeV]. Another result of wrong combinations is the predicted low-mass behavior of $\langle Y_1^0 \rangle$ for R2, R3, and R4: Instead of a steep backward $\langle Y_1^0 \rangle$ as predicted in Fig. 8(a) (a single combination case), we predict only a slightly negative $\langle Y_1^0 \rangle$ below 1.15 GeV. This prediction does not adequately describe the low-mass $\langle Y_1^0 \rangle$ data of R2 and R3,[28] but does represent the data in Fig. 8(d) well, however.

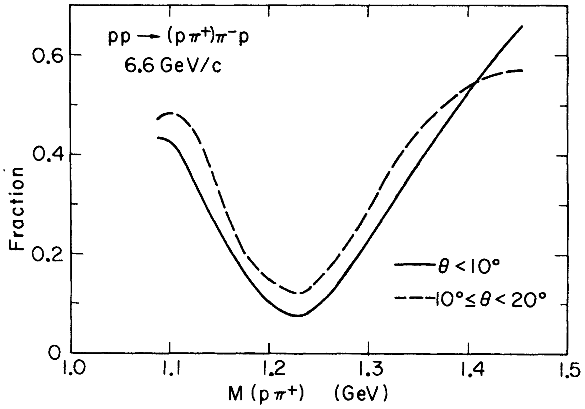

FIG. 13. OPE predictions for the fraction of wrong $p\pi^+$ combinations for R2 plotted as a function of $M(p\pi^+)$ for several bins in θ. The curves are described in Sec. VI.

Thus the difference between the low-mass data of Figs. 8(b), 8(c), and those of Fig. 8(d) may be due to off-mass-shell effects and/or indirect production of $p\pi^+$ systems in R2 and R3 via, e.g., $N^{*+} \to (p\pi^+)\pi^-$; the $p\pi^+$ systems of R4 are produced directly (as in Fig. 12) since the π^- is associated strongly with the final-state neutron via the observed $\Delta^-(1238)$ resonance. In Sec. VII we briefly consider the possibility of indirect production of $p\pi^+$ systems using the data of R2.

VII. A FURTHER LOOK AT R2

In this section we consider further the possible production mechanisms for the R2 data in several bins of θ. Figures 14(a)–14(c) display the $M(p\pi^-)$ spectra for $\Delta^{++}(1238)p\pi^-$ combinations [i.e., combinations with $1.16 < M(p\pi^+) < 1.30$ GeV] in three θ bins. The strong resonant structure observed in Fig. 5(a) is especially enhanced for the very peripheral data in Fig. 14(a); similar structure is also observed in Figs. 14(b) and 14(c). This $M(p\pi^-)$ structure strongly suggests direct $\Delta^{++}(1238)$ production via a process such as displayed in Fig. 12 with $X = p\pi^-$. The smooth curves superimposed upon the data in Fig. 14 represent the absolute predictions of the OPE model described above and in the Appendix: They generally describe the data well in shape but are about 10%

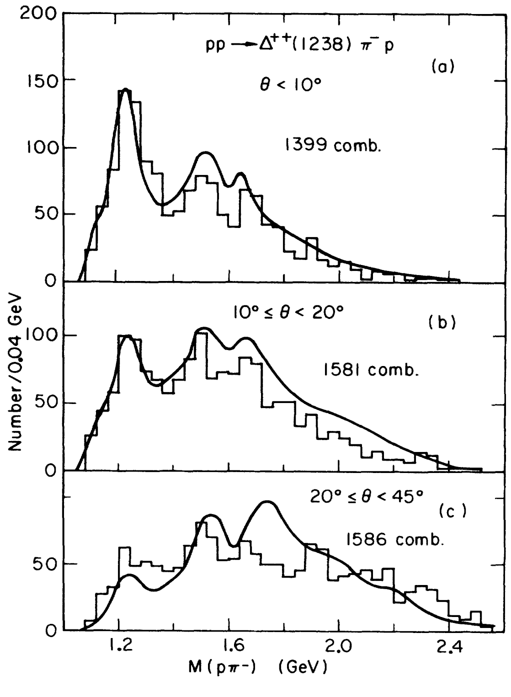

FIG. 14. Distributions of $\pi^- p$ invariant mass for $pp \to \Delta^{++}(1238)\ \pi^- p$ combinations satisfying the denoted θ cuts. The solid curves represent the OPE-model predictions described in Sec. VII.

too high for the $\theta < 20°$ data.[29] We point out that good agreement has also been obtained between the $\pi^- p$ vertex moments ($X = p\pi^-$ in Fig. 12) and the predictions of $\pi^- p$ elastic scattering (cf. Fig. 19 of Ref. 2). This further supports an interpretation of direct production of $\Delta^{++}(1238)$ systems in R2.

We turn now to a consideration of R2 data from the viewpoint of indirect production of $p\pi^+$ systems, i.e., we consider the possibility of direct production of $p\pi^+\pi^-$ systems. This study is performed utilizing four $M(p\pi^+)$ bins below $M(p\pi^+) = 1.48$ GeV and two θ bins below 45°. In Figs. 15(a)–15(d) we show the $M(p_i\pi^+\pi^-)$ spectra for $\theta < 20°$ for the four denoted bins in $M(p_i\pi^+)$; corresponding distributions for $20° < \theta < 45°$ are presented in Figs. 15(e)–15(h), respectively. The vertical arrow drawn in each component figure at an abscissa of 1.7 GeV represents the approximate position of the enhancement seen in the total $M(p\pi^+\pi^-)$ spectrum which accounts for ~10% of the R2 data.[2] The histograms in Figs. 15(a) and 15(d) ($\theta < 20°$) as well as the $20° < \theta < 45°$ data each display a peaking at 1.7 GeV. No visible peaking occurs at 1.7 GeV for the $\theta < 20°$ data with $1.16 < M(p\pi^+) < 1.30$ GeV [the $\Delta^{++}(1238)$ data]. Also to be noted are the usual threshold peaks (1.4–1.6 GeV) in Figs. 15(a)–15(c).

The smooth curves drawn in Figs. 15(a)–15(h) represent the corresponding predictions of the OPE model discussed above and in the Appendix. As stated earlier,[2] the normalizations of the 1.4–1.6 GeV mass enhancements are accounted for by the OPE predictions; the curve shapes are too broad, however. This difficulty is readily eliminated by Reggeization of the exchanged pion.[2,30] The 1.7 GeV mass enhancements observed in Figs. 15(a), 15(d), and 15(h) cannot be accounted for by OPE-model predictions which only utilize the process depicted in Fig. 12. Thus some indirect production of $p\pi^+$ systems with $M(p\pi^+) < 1.16$ GeV and $1.30 \leq M(p\pi^+) < 1.48$ GeV certainly does exist. The corresponding situation for the $1.16 < M(p\pi^+) < 1.30$ GeV data is not clear: There does exist a steep shoulder at ~1.8 GeV in Figs. 15(b), 15(c), 15(f), and 15(g) which suggests some effect, but it is not very strong.

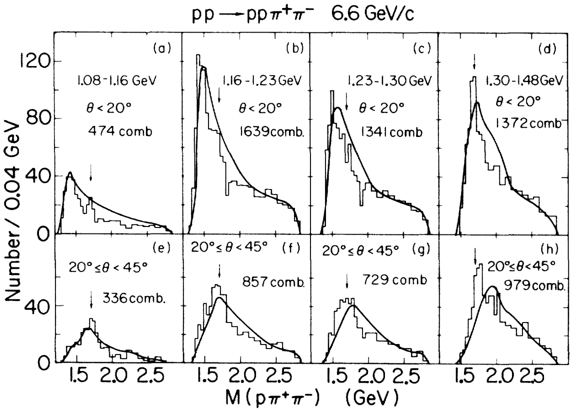

FIG. 15. Histograms of $M(p_i\,\pi^+\pi^-)$ for the denoted cuts on $M(p_i\,\pi^+)$ using data of R2: (a)–(d) refer to $p\pi^+$ systems with $\theta < 20°$; (e)–(h) refer to the corresponding $p\pi^+$ mass cuts but are for $20° \leq \theta < 45°$. The solid curves represent the OPE-model predictions described in Sec. VII.

As to the possibility of indirectly produced $p\pi^+$ systems affecting the $\langle Y_1^0 \rangle$ moments in Figs. 8(b) and 9(b) for $M(p\pi^+) < 1.15$ GeV, there is evidence for $N^*(1700) \to p\pi^+\pi^-$ in these data and it will have an effect. However, embellishments such as Reggeization, absorption, and interferences would also have to be considered for more serious comparisons between data and theory.

VIII. CONCLUSIONS

Peripheral $\Delta(1238)$ isobar production dominates inelastic proton-proton interactions at 6.6 GeV/c. In R1–R4, $\Delta^{++}(1238)$ production is observed for approximately 35%, 80%, 55%, and 50% of the data, respectively. Strong $\Delta^-(1238)$ production, sometimes occurring simultaneously with $\Delta^{++}(1238)$ production, is also present in the R4 data. The $\Delta(1238)$ systems are produced quite peripherally; the degree of peripherality is inversely proportional to the number of final-state particles. The $\Delta(1238)$ decays indicate nonpure partial-wave structure, with contributions from s wave as well as the dominant p wave. The corresponding decay density-matrix elements of all $|T_z| = \frac{3}{2}$ $\Delta(1238)$ systems display a similar trend with increasing c.m. angle: The ρ_{33} all increase smoothly from ~0.10 to ~0.25 in going from 0° to 90°; with exception of R1 the $\mathrm{Re}\rho_{3,1}$ are generally small and negative, and the $\mathrm{Re}\rho_{3,-1}$ are consistent with zero.

Detailed analyses of the πN mass dependence of the peripheral ($\theta < 20°$) t-channel moments $\langle Y_L^0 \rangle$ and $\langle \mathrm{Re}Y_L^M \rangle$ indicate significant differences between the $T_z = +\frac{3}{2}$ and $T_z = -\frac{3}{2}$ data. These differences, as well as the mass dependences of the R1–R4 $p\pi^+$ moments, can be interpreted simply in terms of direct production of $p\pi^+$ systems via the peripheral OPE process depicted in Fig. 12, at least in the region of the $\Delta^{++}(1238)$ (1.16–1.30 GeV). Moreover, the approximate description of the $M(p\pi^-)$ spectra for the peripheral $pp \to \Delta^{++}(1238)$ $p\pi^-$ events by the corresponding OPE-model predictions further supports the direct production hypothesis for R2. Similar production mechanisms for $\Delta^{++}(1238)$ systems in R3 and R4 are then suggested by our earlier comparisons[1] between systems recoiling against a peripheral $\Delta^{++}(1238)$ in R2–R4.

In conclusion peripheral $\Delta^{++}(1238)$ production in R1–R4 can be mainly understood in terms of direct $\Delta^{++}(1238)$ production via OPE processes. R2 and R3 studies with $M(p\pi^+) < 1.16$ GeV or $M(p\pi^+) > 1.3$ GeV must additionally consider indirect $p\pi^+$ production via, e.g., $N^*(1700) \to p\pi^+\pi^-$. Models attempting to interpret the R2–R4 data should certainly consider both $p\pi^+$ combinations, especially if data outside of the very peripheral ($\theta < 10°$) $\Delta^{++}(1238)$ peak region are to be studied. Finally, serious theoretical comparisons would require explicit consideration of off-mass-shell effects [largest for small $M(p\pi^+)$], absorption (especially for R1), Reggeization, and interferences neglected in this work.

ACKNOWLEDGMENTS

We thank Eugene Gellert and Professor Z. Ming Ma, Professor P. E. Schlein, and Professor G. A. Smith for their participation in the early stages of this experiment. One of us (E. C.) appreciates the comments of Dr. F. Muller and Dr. G. Smadja. Of course this experiment would not have been possible without the efforts of Robert Watt and the entire crew of the 72-in. bubble chamber.

APPENDIX

In this section we describe the OPE calculations whose results are described in Secs. V–VIII. The cross section σ for a scattering process giving rise to n particles in the final state can be expressed[31] as

$$\sigma = \frac{(2\pi)^4}{4m_p P_L (2\pi)^{3n}} \int \sum_{\text{spins}} |M|^2 dR_n , \qquad \text{(A1)}$$

where P_L is the laboratory momentum, M is the invariant amplitude for the process, and R_n represents Lorentz-invariant n-body phase space.[32] For pp peripheral OPE processes M represents the coherent sum of four terms corresponding to interchanges of initial-state protons and/or final-state nucleons. At our beam energy interferences between amplitudes representing interchanges of initial protons or final-state nucleons is small and can be neglected. For simplicity we further neglect the interference between amplitudes representing processes differing by interchange of both initial-state protons and final-state nucleons. Figure 2(a) indicates that interferences should be considered for any serious data-to-model comparisons, however.

Therefore, we consider only the peripheral OPE process displayed in Fig. 12 and we write[33]

$$\sum_{\text{spins}} |M|^2 = 2\times 64\pi^2 \left(M^2(p\pi^+) \frac{Q_t}{Q} \frac{d\sigma}{d\Omega}(M(p\pi^+), t) \right) \times \frac{1}{(t-\mu^2)^2} G(M(X), t, \Omega_X), \qquad \text{(A2)}$$

where Q_t (Q) is the incoming (outgoing) momentum evaluated in the $p\pi^+$ rest system, t is the four-momentum transfer squared to the $p\pi^+$ system, and $d\sigma(M(p\pi^+), t)/d\Omega$ is the off-mass-shell differential cross section at the upper vertex in Fig. 12. The off-mass-shell vertex function G represents $\pi^- p$ elastic (R2) or inelastic (R3, R4) scattering at the lower vertex in Fig. 12.

In evaluating $\sum |M|^2$, the $p\pi^\pm$ elastic scattering vertex functions were modified for use in the physical region of t with Benecke-Dürr[34] off-shell corrections multiplying the on-shell values; for the R parameters we used Wolf's[35] determinations. However, no off-shell corrections were applied for $M(p\pi^\pm) > 1.6$ GeV,[36] and also no off-shell corrections were made to inelastic scattering vertex functions; in these cases we simply used the on-shell functions in (A2). The on-shell differential cross sections for $p\pi^\pm$ elastic scattering were reconstructed from the CERN phase shifts[21]; the $\pi^- p$ inelastic scattering differential cross sections utilized the data of Brody *et al.*[37] Following Wolf[35] we set the vertex functions to zero for $|t| > 1$ GeV^2.

Equation (A1) was integrated by utilizing a Monte Carlo technique[27] with preferred phase-space generation. Events were generated using the program SAGE.[38] The event weight, corresponding to the product of the phase-space weight and the evaluation of $\sum |M|^2$ [by Eq. (A2)] for that event, was computed and summed over all events, thus performing the integration. For further calculations of moments, etc., we used unweighted Monte Carlo events.[39] Thus, the curves appearing in Figs. 8–11 and 13–15 (R2–R4 only) were obtained by using only $p\pi^+$ combinations (just as in the real data) which satisfied the denoted $M(p\pi^+)$ and θ selections.

---

*Work supported by the U. S. Atomic Energy Commission.

[1] E. Colton *et al.*, Phys. Rev. Letters 21, 1548 (1968); Phys. Rev. D 2, 2108 (1970).

[2] E. Colton *et al.*, Phys. Rev. D 3, 1063 (1971).

[3] W. E. Ellis *et al.*, Phys. Letters 32B, 140 (1970).

[4] T_z represents the z component of isotopic spin of the pion-nucleon system.

[5] W. Chinowsky *et al.*, Phys. Rev. 165, 1466 (1968).

[6] E. Colton, Ph.D. thesis, University of California, Los Angeles, Report No. UCLA-1025, 1968 (unpublished).

[7] See, e.g., J. D. Jackson, Nuovo Cimento 34, 1644 (1964).

[8] See, e.g., F. Solmitz, Ann. Rev. Nucl. Sci. 14, 375 (1964).

[9] Phillippe Eberhard and Werner Koellner, LRL Report No. 20160, 1971 (unpublished).

[10] Figure 5 will indicate clear resonance production in the $M(\pi^- p)$ spectrum of R2. A really correct determination of resonance cross sections requires a detailed t-dependent model involving interference effects, which is beyond the scope of this work.

[11] Best fit masses and widths are first obtained for the resonances in a preliminary fit; then the partial fractions are obtained in a second fit where the best fit masses and widths are held fixed.

[12] Particle Data Group, Rev. Mod. Phys. 43, S1 (1971).

[13] K. Gottfried and J. D. Jackson, Nuovo Cimento 33, 309 (1964).

[14] In the conventional t-channel coordinate system, the incident proton as seen in the $\Delta(1238)$ rest frame is taken as the polar or z axis, the y axis is along the normal to the production plane $\hat{y} = \hat{n} \sim \hat{P}_p \times \hat{P}_\Delta$. The transformation to the s channel or helicity system results from using the $\Delta(1238)$ direction in the over-all c.m. frame as the z axis.

[15] To calculate $\langle Y_L^M \rangle$ we simply average Y_L^M over the $\Delta(1238)$ events, defined by Eq. (3.1), for each θ bin considered.

[16] Since $\Delta^{++}(1238)$ production is dominantly peripheral, combinations are weighted according to the value of the c.m. angle θ.

[17] See, e.g., J. D. Jackson, Rev. Mod. Phys. 37, 484 (1965).

[18] See, e.g., J. D. Jackson, invited paper, in Proceedings of the Stony Brook Conference on High-Energy Two-Body Reactions, 1966 (unpublished).

[19] This is true if the y axis is taken to be the normal to the production plane.

[20] See, e.g, G. F. Chew and F. E. Low, Phys. Rev. 113, 1640 (1959).

[21] A. Donnachie, R. G. Kirsopp, and C. Lovelace, CERN Report No. CERN-TH-838, Addendum, 1967 (unpublished).

[22] This effect can be partly explained by off-mass-shell effects. See, e.g., Eugene Colton and Peter E. Schlein, in *Proceedings of a Conference on $\pi\pi$ and $K\pi$ Interactions at Argonne National Laboratory, 1969,* edited by F. Loeffler and E. D. Malamud (Argonne National Laboratory, Argonne, Ill., 1969), p. 1.

[23] This effect may be analogous to the observed depolarization of the ρ^0 produced in $\pi^- p \rightarrow \rho^0 n$. In this case nonzero helicity states of the ρ^0, forbidden by simple OPE, but allowed by the absorption model, occur.

[24] Z. Ming Ma *et al.*, Phys. Rev. Letters 23, 342 (1969).

[25] Specifically, the correct $p\pi^+$ combination is depicted as emerging from the upper vertex of Fig. 12; the wrong $p\pi^+$ combination, in the cases of R2 and R3, is the observed π^+ taken with the proton of the X system at the lower vertex. In the case of R4 the observed outgoing proton (in Fig. 12) taken with the π^+ of the X system represents the incorrect combination.

[26] Inclusion of interferences into the calculations would produce large increases in computation time. Moreover, it is our purpose here to establish trends in the data, not to test some complicated (and still imprecise) theoretical model.

[27] J. H. Friedman, J. Comp. Phys. 7, 1 (1971).

[28] Our earlier analysis of R2 (Ref. 2), which did not consider wrong combinations, ascribed this discrepancy mainly to off-mass-shell effects.

[29] The use of a mild t-dependent form factor (to approximately compensate for absorption effects) in the OPE calculations presumably would bring about very good agreement; see Ref. 2.

[30] E. L. Berger *et al.*, Phys. Rev. Letters 20, 964 (1968).

[31] See, e.g., M. Jacob and G. Chew, *Strong Interaction Physics* (Benjamin, New York, 1964), Chap. 1.

[32] See, e.g., R. Hagedorn, *Relativistic Kinematics* (Benjamin, New York, 1963), Secs. 7-4 and 7-5.

[33] See, e.g., E. Ferrari and F. Selleri, Nuovo Cimento, Suppl. 24, 453 (1962).

[34] J. Benecke and H. P. Dürr, Nuovo Cimento 56, 269 (1968).

[35] G. Wolf, Phys. Rev. 182, 1538 (1969).

[36] The off-shell corrections are greatest for small mass and large $|t|$. See Ref. 2.

[37] A. D. Brody *et al.*, Phys. Rev. D 4, 2693 (1971).

[38] Jerry Friedman, Group A Programming Note P-189 (Rev), 1971 (unpublished).

[39] The generation of unweighted events is accomplished by generating a random number w (for each event) in the interval $(0, w_{\max})$ where $w_{\max}$ is an upper bound for the event weights. Events having weight less than w are discarded; those not discarded are given unit weight.